Electrochimica Acta 104 (2013) 94–103

Contents lists available at SciVerse ScienceDirect

Electrochimica Acta

journal homepage: www.elsevier.com/locate/electacta

Structural, magnetic, and mechanical properties of electrodeposited cobalt–tungsten alloys: Intrinsic and extrinsic interdependencies

N. Tsyntsaru[a,b,*,1], H. Cesiulis[c], E. Pellicer[d], J.-P. Celis[b], J. Sort[e]

[a] Institute of Applied Physics of ASM, 5 Academy str., Chisinau, MD-2028, Republic of Moldova
[b] KU Leuven, Dept. MTM, Kasteelpark Arenberg 44, B-3001, Belgium
[c] Vilnius University, Dept. Phys. Chem., Naugarduko 24, Vilnius LT-03225, Lithuania
[d] Departament de Física, Facultat de Ciències, Universitat Autònoma de Barcelona, E-08193 Bellaterra, Spain
[e] Institució Catalana de Recerca i Estudis Avançats (ICREA) and Departament de Física, Universitat Autònoma de Barcelona, E-08193 Bellaterra, Spain

ARTICLE INFO

Article history:
Received 31 March 2013
Accepted 3 April 2013
Available online xxx

Keywords:
Co–W alloys
Electrodeposition
Hardness
Magnetization
Crystallite size

ABSTRACT

The mapping of structural, magnetic, and mechanical properties of Co–W coatings galvanostatically electrodeposited from a citrate–borate bath is investigated. The intrinsic characteristics of the coatings, such as crystallite size or tungsten content are correlated with the extrinsic growth parameters, such as pH, complexes distribution, and current density. The increase in pH from 5 to 8 results in an increase of the W content in the deposits from 2 at.% up to 36 at.% in a controlled way, and it correlates with an increase in concentration of W(VI) complexes in the bath. The crystallite size estimated from XRD patterns, decreases from 39 to 5 nm with increasing W content from 3 to 25 at.% respectively. The obtained coatings show highly tunable mechanical and magnetic properties. The hardness increases with W content from ~3 GPa up to ~13 GPa. A semi-hard ferromagnetic behavior with a coercivity of ~470 Oe along the perpendicular-to-plane direction is observed for Co–W alloys containing small amounts of W in the range of ~2–3 at.%. At higher tungsten contents the coatings are magnetically softer, and the electrodeposits become non-ferromagnetic beyond ~30 at.% W. Because of this combination of physical properties, electrodeposited Co–W coatings may become suitable materials for multi-scale technologies.

1. Introduction

Nowadays theoretical and practical studies on the Co-deposition of tungsten with iron group metals, Me–W, where Me = Co, Ni or Fe, are conducted worldwide [1–3]. That research is encouraged by the outstanding mechanical, tribological, and magnetic properties as well as the corrosion resistance of tungsten alloys [3]. The magnetic properties of electrodeposited Me–W alloys are of interest in recording media [4,5] and remotely-actuated micro-/nano-electromechanical systems (MEMS/NEMS), such as microactuators, micromotors, sensors, microgears or micromechanical magnetometers [6–8]. Often, materials used in magnetic applications need to possess additional functional features such as mechanical properties at high temperatures and/or corrosion resistance [6,9]. Owing to this combination of properties, electrodeposited Me–W alloys are suitable candidates to meet these technological demands.

The mapping of the alloy properties is a critical step towards an implementation of such materials in devices. Indeed such a mapping is important to establish interdependencies between intrinsic and extrinsic properties/parameters. It is well known that the key factor determining the structure and properties of an alloy is its chemical composition. In that respect, the saturation magnetization, M_S, can be considered as an intrinsic property [9,10] independent of grain size and microstructure, and dependent only on the composition of the alloy. Conversely, coercivity, H_C, and remanence, M_r, can be regarded as extrinsic properties [9,10] dependent both on grain size and microstructure, as well as on grain shape, texture, and internal stress. The intrinsic and extrinsic material properties are linked to the electrodeposition conditions like current density or deposition potential, pH, and plating temperature which, in turn, determine the intrinsic deposit properties such as alloy composition, microstructure, and crystallite size.

Depending on the electrodeposition conditions, Co–W coatings can exhibit either hard or soft ferromagnetic properties [11,12]. Remarkably, even if the alloy composition does not vary significantly with current density, *i*, the microstructure of the coatings becomes progressively more refined as the absolute value of *i*

* Corresponding author at: Institute of Applied Physics of ASM, 5 Academy str., Chisinau, MD-2028, Republic of Moldova. Tel.: +37 322731725.
E-mail addresses: tintaru@phys.asm.md, ashra_nt@yahoo.com (N. Tsyntsaru), henrikas.cesiulis@chf.vu.lt (H. Cesiulis), eva.pellicer@uab.cat (E. Pellicer), jean-pierre.celis@mtm.kuleuven.be (J.-P. Celis), jordi.sort@uab.cat (J. Sort).
[1] ISE member.

0013-4686/$ – see front matter © 2013 Elsevier Ltd. All rights reserved.
http://dx.doi.org/10.1016/j.electacta.2013.04.022

increases, leading to a pronounced variation of the properties such as coercivity and squareness ratio, M_R/M_S. The formation of hard-magnetic hcp Co_3W is usually promoted in coatings electrodeposited at low i [11], whereas amorphous Co–W coatings with low coercivity both along in-plane and perpendicular-to-plane directions are obtained at high current densities. The coercivity of Co_3W coatings also depends on the texture degree [11]. Typically, a (0 0 1) texture developed during the growth of Co_3W hcp coatings, favors hard ferromagnetic behavior and perpendicular-to-plane magnetic anisotropy [8]. Conversely, fcc and amorphous Co–W are magnetically softer [8,11,12]. As expected, the saturation magnetization of Co–W alloys tends to decrease with increasing W percentage [11]. However, a further lowering of M_S with the W content is observed when coatings become amorphous [12].

As aforementioned, a combination of suitable magnetic properties with excellent mechanical behavior is required in the case of high-density magnetic recording media. Indeed, an outstanding wear resistance is indispensable since the read heads fly at only a few nm above the surface of the hard disk [13]. In this sense, magnetic alloys containing refractory metals, such as Co–W, possess a unique combination of mechanical and tribological properties. Co–W coatings apparently possess the lowest wear rate among the binary Me–W alloys, and their hardness is comparable to that of electroplated chromium [14]. As-deposited Co–W coatings exhibit hardness, coefficient of friction, and wear resistance, which depend on the electrodeposition conditions [14–19]. On the other hand, the intrinsic coating characteristics such as grain size, dislocation density, crystal structure, roughness, and film thickness govern the mechanical properties and the material deformation mechanisms [9].

The aims of this work are to map the magnetic and mechanical properties of Co–W coatings electrodeposited from a citrate–borate bath, and to act on their microstructural features in order to improve their magnetic/mechanical performance.

2. Experimental

Co–W coatings were obtained by electrodeposition under galvanostatic mode from a citrate–borate electrolyte containing (mol L^{-1}) [16]: $CoSO_4$ – 0.2; Na_2WO_4 – 0.2; $C_6H_8O_7$ – 0.04; $Na_3C_6H_5O_7$ – 0.25; H_3BO_3 – 0.65. The pH was adjusted to 5.0, 6.7 or 8.0 by the addition of H_2SO_4 or NaOH. The plating temperature was kept at 60 °C. Pure Co coatings were electrodeposited from the same solution but free of Na_2WO_4 operated at pH 6.7, and at a cathodic current density of 10 mA cm^{-2}. Preliminary results on the effect of coating thickness, t, on the magnetic properties of Co-based alloys showed that these properties are strongly affected at low thicknesses ($t < 1$ μm) but tend to stabilize at higher thicknesses [12,20–22]. Therefore, relatively thin coatings of ca. 2 μm were electrodeposited for magnetic measurements. Thicker coatings of about 9 μm were electroplated to accurately measure the hardness of the coating without any influence of the substrate (the indentation depth should be less than 1/10 of the overall coating thickness). The thickness of the electrodeposits was calculated from gravimetric and elemental analysis data. A galvanostat/potentiostat AUTOLAB 302 in combination with the software GPES was employed.

The calculation of species distribution in the electrolyte was done based on available equilibrium constants for acids including tungstic acid and tungstates [23,24], and stability constants of various Co(II) and mixed tungstate–citrate complexes $[(WO_4)_p(HCit)_qH_r]^{(2p+3q-r)-}$ [25].

The surface morphology of the coatings was investigated by scanning electron microscopy (SEM Philips XL 30 FEG) equipped with energy dispersive X-ray spectroscopy (EDX) and a super-ultra-thin window. Cross-sections were prepared by focused ion beam (FIB) to reveal the characteristic growth of the coatings. X-ray diffraction patterns were recorded in a diffractometer (DRON-3.0) with Bragg–Brentano geometry and using a Ni filtered Cu-K_α radiation (λ = 1.54183 Å) operated at 30 kV and 30 mA at a constant scan speed of 0.02° 2θ s^{-1}.

The electrodeposition was performed in a standard 3-electrodes electrochemical cell. A platinum mesh served as anode, while a 3 M Ag/AgCl electrode was used as reference electrode. All potentials in this study are referred to this electrode. All electrodeposition tests were done on a stationary copper working electrode except for nanoindentation measurements for which flat Si coupons with copper seed-layer were used. The surface roughness of substrate and as-deposited coatings was determined by non-contact white light interferometry (WYKO NT 3300).The Si/Cu substrates had a low roughness, Ra ~ 6 nm. Prior to mechanical testing, the as-deposited Co and Co–W samples were polished to achieve a roughness Ra ~100 nm. Hardness and elastic modulus were determined by the method of Oliver and Pharr [26] applied on nanoindentation tests (nanohardness tester, CSM). These tests were performed using a diamond Berkovich indenter at normal loads of 20 mN and 80 mN. The hardness values reported are the statistical average of 5 indentations.

Magnetization hysteresis loops were measured on as-deposited samples at room temperature with a vibrating sample magnetometer (Oxford Instruments 1.2 VSM) applying the magnetic field both along in-plane and perpendicular-to-plane directions (maximum applied field of 1 T).

3. Results and discussion

3.1. Electrodeposition parameters and bath influence on alloy composition

The dependence of tungsten content in Co–W alloys on the cathodic current densities shown in Fig. 1 for different solution pHs. We considered the composition of the electrodeposited alloys as fractions of metallic phases only, although some oxygen and carbon were also detected. The presence of such non-metallic elements in electrodeposited tungsten alloys was reported and discussed earlier [16,27,28]. Moreover, the activation energy for desorption of oxygen from tungsten surface is high, namely 269–480 kJ/mol [29]. Therefore oxygen forms a strongly bonded layer on the surface of tungsten. Also, water can act as an oxidizing agent of tungsten [2]. However the level of non-metals incorporated into the

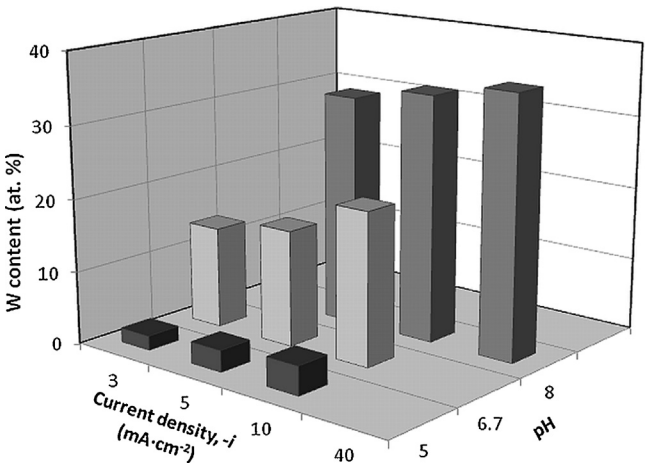

Fig. 1. Mapping of the composition of Co–W electrolytic coatings with pH and current density.

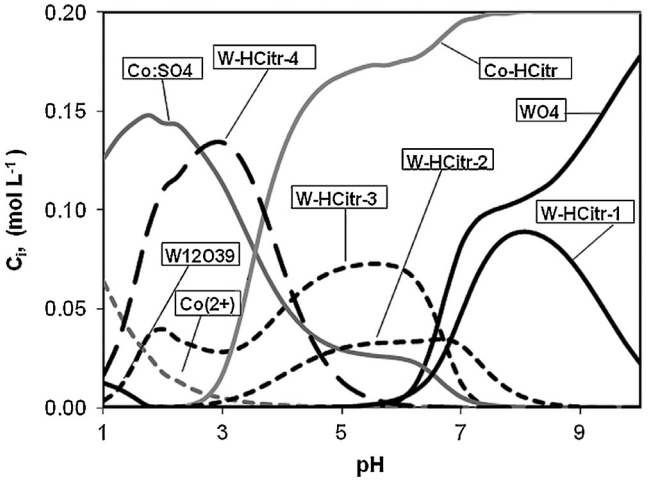

Fig. 2. Calculated concentrations of main species (C_i) as a function of pH in a solution containing 0.2 M $CoSO_4$, 0.2 M Na_2WO_4 and 0.3 M citrates.
Nomenclature: WO_4 is WO_4^{2-}; W-HCitr-1 is $[(WO_4)(HCitr)H]^{4-}$; W-HCitr-2 is $[(WO_4)(HCitr)H_2]^{3-}$; W-HCitr-3 is $[(WO_4)_2(HCitr)H_4]^{3-}$; W-HCitr-4 is $[(WO_4)(HCitr)H_3]^{2-}$; $W_{12}O_{39}$ is $[W_{12}O_{39}]^{6-}$; C(2+) is Co^{2+}; Co:SO_4 is Co^{2+}:SO_4^{2-}(ionic pair); Co-HCitr is $[Co(HCitr)]^{-}$.

coatings in this research did not affect the resulting ratio of metallic components in the coatings. At a given cathodic current density the tungsten content in the electrodeposit increases with increasing pH. To some extent, this result correlates with the changes in "bath chemistry" as a function of pH shown in Fig. 2. Different complexes with citrates, hydroxocomplexes, citrate–tungstate complexes are formed in Co–W solutions. The distribution of the main Co(II) and W(VI) species in the citrate–borate solutions are also shown in Fig. 2. Since the concentrations of other forms of Co(II), such as hydroxo-complexes or hydrocitrate complexes, and polytungstates are much lower, they are not shown in Fig. 2. In the pH range of 1–10, two main forms of Co(II) exist in solution, namely as ionic pair Co^{2+}:SO_4^{2-} and as citrate complex. The concentration of "free" Co^{2+} becomes significant only at pH < 3. These two main Co(II) species are likely responsible for the fast formation of electrochemically active $CoOH^+$ species, allowing a relatively high partial current density (PCD) for Co in the whole range of pH. The increase of the W percentage in the alloy with pH correlates well with the rapid raise in the concentration of some W(VI)–citrate complexes such as $(WO_4)(HCitr)H^{4-}$ at pH > 5. This feature also explains the small increase of the tungsten content noticed in thick coatings in comparison with thin coatings electrodeposited at pH 6.7. Alkalization at the near-electrode zone due to hydrogen evolution during extended electrolysis duration, leads to a small tungsten increase in the coating, probably due to the r ise in concentration of W(VI)–citrate complexes. In turn, the decrease in tungsten content for thick Co–W coatings at pH 8 is ascribed to the drop in $(WO_4)(HCitr)H^{4-}$ concentration (Fig. 2) due to a further alkalization at the near-electrode zone. A similar trend, namely the decrease of the W content at high pH, was also reported in Co–W coatings deposited from a citrate–ammonia electrolyte [30]. Thus, by changing the pH from acidic to alkaline values, it is possible to control and to tune the tungsten content more precisely than what was achieved in previous work done at 6.7–8 [31].

3.2. Mapping of structural properties

The surface morphology, smoothness, and brightness of electrodeposited Co–W coatings were found to vary with cathodic current density, pH, and coating thickness (Fig. 3). Co–W alloys electrodeposited at relatively low current densities and pH 5, are rough

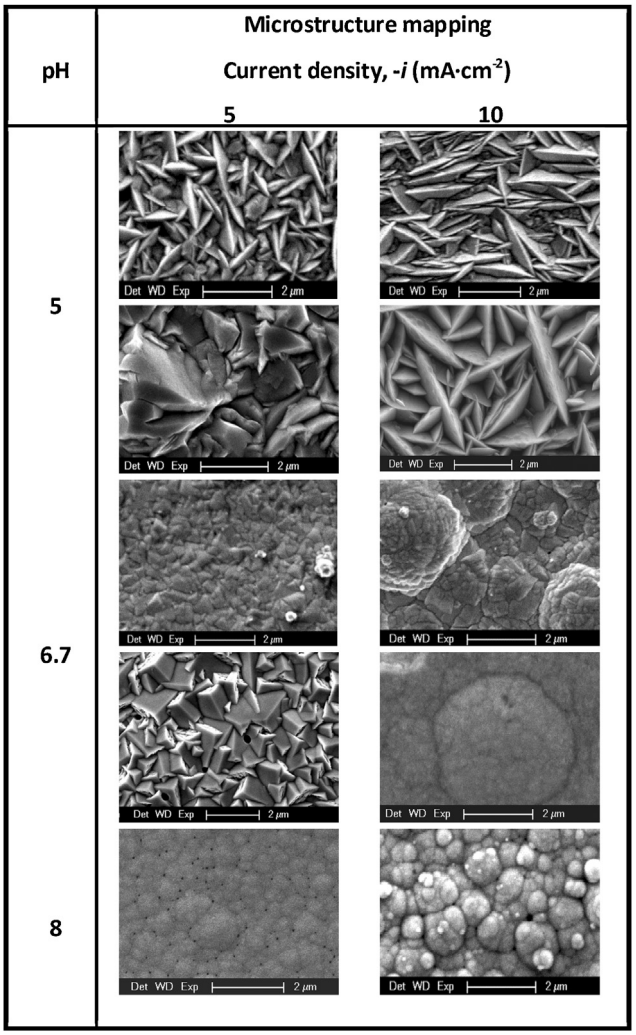

Fig. 3. Mapping of the microstructure of Co–W coatings electrodeposited at different pHs and current densities.

and consist of acicular-shaped grains, whereas at higher current densities, where tungsten-rich alloys (>13 at.% W) are obtained, the surface becomes finer, and the coating appearance is semi-bright. In order to verify whether this is linked to electrochemical nucleation and grain growth processes, cross-sections were examined. A V-shape columnar growth was observed in alloys containing low tungsten content (~3 at.% W) obtained at pH 5 (Fig. 4). A coarse-grained structure perpendicular to the substrate plane is clearly visible in such Co–W electrodeposits. A less pronounced columnar growth is appearing in pure electrodeposited Co. This is in line with previous researches showing that columnar or nanofiber growth was noticed in Ni–W, Ni–Mo, and pure Ni electrodeposits [32,33]. At higher pH and current densities, nucleation dominates over-growth in the case of Co–W (Fig. 3), since cross-section do not reveal a clear granular structure.

The different growth modes as a function of the tungsten content are noticed also affecting the XRD patterns for thin (~2 μm) and thick (~9 μm) Co–W coatings (Fig. 5). Notice that the tungsten content range shown in each row corresponds to coatings deposited under an identical electroplating conditions. A well-defined crystalline structure is obtained when the tungsten content is below 21 at.%. As expected, such Co–W coatings have a hexagonal close-packed (hcp) structure typical for electrodeposited pure Co. An interesting case are the coatings deposited at 10 mA cm^{-2} and pH 6.7 which contain 21 at.% W at a thickness of 2 μm, but a slightly

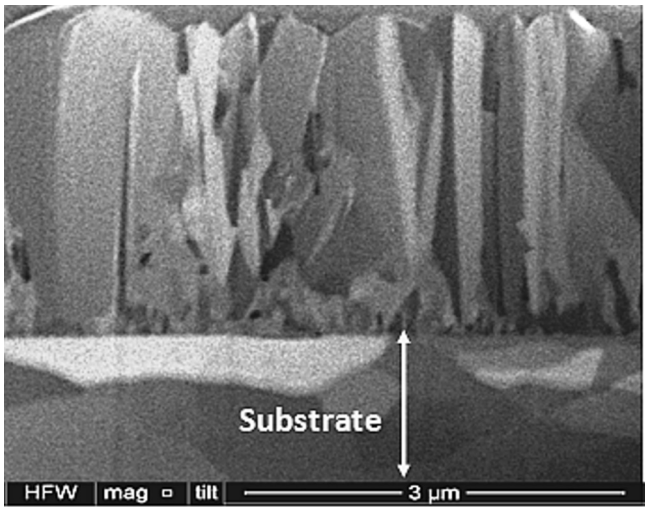

Fig. 4. FIB cross-section of a Co–W alloy containing 3 at.% W and electrodeposited at pH 5.

higher amount of tungsten (24 at.%) at a thickness of 9 μm. Two XRD peaks are recorded on thin ones whereas a single broader peak due to an overlapping of hcp-Co and Co_3W phases is recorded on thick samples. Such a broadening is attributed to the decrease in crystallite size [32,34]. As reported earlier [27], electrodeposited tungsten alloys with Ni, Co or Fe can form thermodynamically stable intermetallic compounds like Ni_4W, Co_3W and Fe_2W, which are usually amorphous-like and hard. Indeed, electrodeposited Me–W alloys containing 20–35 at.% W are reported to be either amorphous

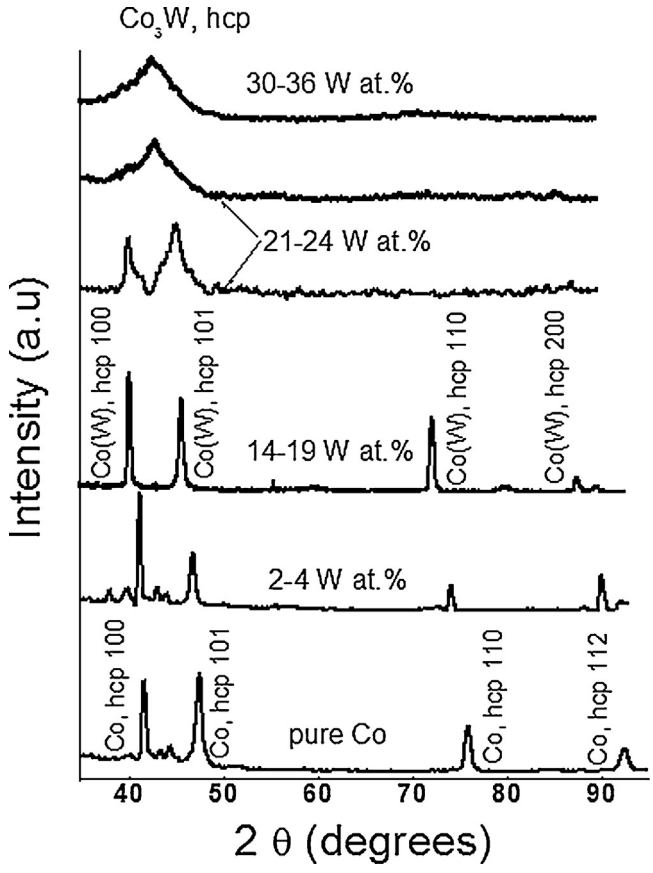

Fig. 5. X-ray diffraction patterns recorded on Co–W electrodeposits with a different W content.

[35,36] or nanocrystalline with crystallite sizes smaller than 5 nm for Co–W [14] and Fe–W [28]. The transition from relatively coarse grains to nanocrystallites takes place in a narrow range of tungsten content, namely between 18 and 22 at.% W [31]. Hence, the effect of thickness on the structure of coatings deposited at 10 mA cm^{-2} and pH 6.7, can result from a slight variation in coating composition due to an alkalization of the near electrode layer. Such an effect is more pronounced for thick coatings, thus facilitating the reduction of tungstates and the concomitant increase in W content.

The peak height ratios in Fig. 5 for electrodeposited Co and Co–W differ from those tabulated in the *JCPDS Cards*, indicating the existence of a preferred crystallographic texture. For example, the Bragg peak associated to {0 0 2} planes is virtually not seen for any of the coatings in this study. In addition, according to the *JCPDS Cards*, the intensity of the {1 0 0} peak in non-textured hcp-Co should be only 1/5 of that of the {1 0 1} peak. Hence, a clear {1 0 0} texture is obtained in the herein investigated Co and Co–W films. The ratio of peaks intensity defines a texture fraction, f_i, that can be estimated from:

$$f_i = \frac{I_j/I_{0,j}}{\sum_j I_j/I_{0,j}} \quad (1)$$

with I_j and $I_{0,j}$ (where $j=(h\,k\,l)$) the experimental and tabulated peak intensities respectively.

Based on the intensity ratios of XRD reflections, the calculated fraction of {1 0 0} texture in hcp Co–W alloys is as high as 66 up to 81% while the theoretical fraction is ~30%.

Notably, for Co–W coatings containing more than 14 at.% W, the XRD peak angular positions attain values characteristic for Co_3W alloy. On the one hand, according to the *JCPDS cards*, the difference in peak positions for hcp Co {1 0 0}, {1 0 1} and Co_3W {2 0 0}, {2 0 1} are ~1°. On the other hand, the solubility limit of W in Co is 17.5 at.% [2]. Hence, the formation of a solid solution is expected at W contents up to this value. In this case, since cobalt atoms in the lattice are substituted by bigger tungsten atoms, an increase in the average closest distance, x_m, between two adjacent atoms should be [31,37,38]:

$$x_m = 2[r_{Co} + (r_W - r_{Co})X_W] \quad (2)$$

with r_{Co} and r_W the atomic radii of cobalt and tungsten, respectively, and X_W the atomic fraction of W in the alloy.

The x_m value is related to the peak position, Θ_m, in accordance with Scherrer's equation:

$$x_m = \frac{1.23\lambda}{2\sin\ \Theta_m} \quad (3)$$

with λ the wavelength.

Therefore, the increase in x_m shifts the peak position 2θ towards smaller angles [38]. Indeed, calculations using Eqs. (2) and (3) show that for Co–W alloys having 13–15 at.% W, the $2\Theta_m$ peak positions for hcp Co and for Co_3W totally overlap. Therefore, at this range of W content, the hcp structure of Co where some Co atoms are replaced by W (solid solution) can be assumed, although the presence of some Co_3W clusters cannot be ruled out.

For coatings containing 17–21 at.% W, it is rather difficult to elucidate which of the two possible hcp phases, namely cobalt–tungsten solid solution in the hcp-Co phase or the hcp-Co_3W phase, has been deposited. If the first one is present, then a supersaturated solid solution of W in Co should be formed. In the second case, Co would partially substitute W in Co_3W since, according to the XRD patterns, the lattice constants derived from peak positions are lower than those for stoichiometric Co_3W (PDF No. 65-3520 [31]).

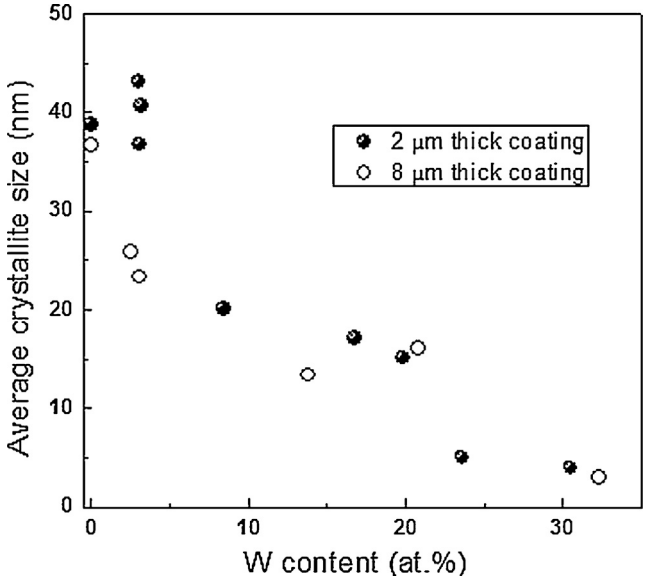

Fig. 6. Effect of tungsten content and coating thickness on the average crystallite size of Co–W alloys.

The evaluation of the crystallite size is of great importance for the understanding of the magnetic [39] and mechanical properties [40,41]. From a comparison of different approaches for XRD investigation [42], it appears that the Williamson–Hall method leads to overestimated grain sizes if microstrains are sufficiently high. On the other hand, the values of crystallite size determined using the Scherrer's equation can vary dependently on the peak considered for calculations. This was the case, for example, for electroplated Ni–W [43], and such an effect is also appearing on analysing the XRD patterns recorded on Co–W electrodeposits. Finally, the crystallite size has been weighted in this study according to the relative texture weight in the diffractograms, as was already successfully applied in [44]. The following equation for crystallite size, τ, weighting was used:

$$\tau_{ave} = \sum_j f_j \tau_j \quad (4)$$

with τ_j the crystallite size of the corresponding $j = h\,k\,l$; and f_i as defined by Eq. (1).

The crystallite size for each peak (actually for each $h\,k\,l$) was estimated from the peak width and angular position using the Scherrer's equation modified by Warren and Biscce [45]:

$$\beta = \frac{0.94\lambda}{\tau_j \cos \Theta_m} \quad (5)$$

$$\beta^2 = B^2 - b^2 \quad (6)$$

with β the peak broadening (in radians), λ the wavelength (in nm), τ the grain size (in nm), Θ_m the peak position, b the peak width for a standard crystalline material (MgO), and B the peak width of the sample analyzed.

The obtained average crystallite size as a function of the tungsten content for 2 μm and 9 μm thick coatings is shown in Fig. 6. All electrodeposited coatings are nanocrystalline. Some differences in crystallite sizes between thin and thick coatings are obtained in alloys containing up to 5 at.% W which consist of a hcp solid solution of Co and W. Probably, an initial nucleation on foreign substrate and the incorporation of tungsten refines the columnar grain structure and introduces more lattice defects what results in a widening of XRD peaks of thin coatings due to both decreasing of grain size and increasing of internal stress, and in a bit lower calculated crystallite size.

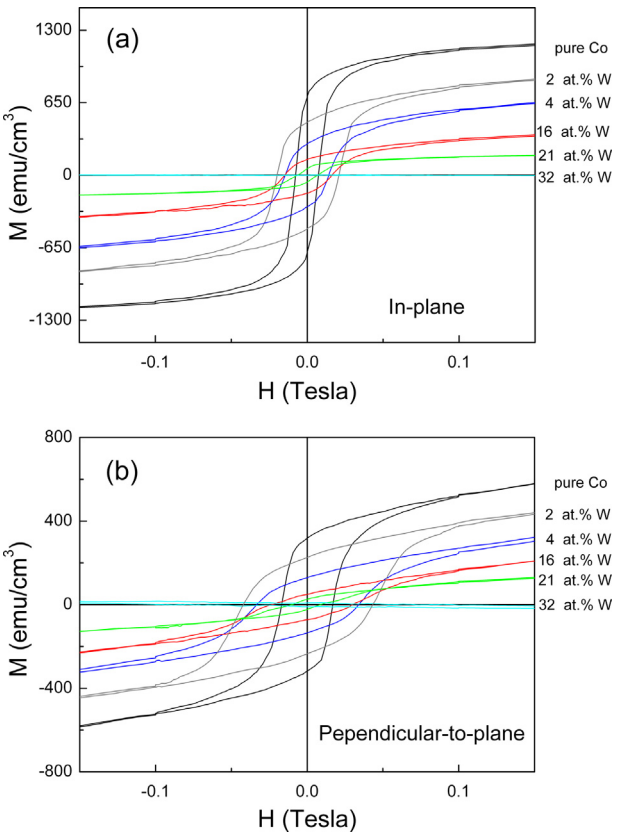

Fig. 7. Hysteresis loops recorded on Co–W coatings on applying the external magnetic field along (a) the in-plane direction, and (b) the perpendicular-to-plane direction.

3.3. Mapping of magnetic properties

While magnetic recording media is composed of hard or semi-hard ferromagnetic or ferrimagnetic materials, magnetic MEMS devices, such as microactuators, frictionless microgears, sensors, or micromotors are constituted of both magnetically hard and soft electrodeposited components [7]. In this work, the magnetic properties of electrodeposited Co–W films have been studied over a wide range of alloy compositions (Fig. 1). VSM measurements reveal that the Co–W coatings with a W content beyond ~30 at.% are non-ferromagnetic, whereas clear hysteresis loops are observed at lower W percentages (Fig. 7). This behavior is linked to the intrinsic properties of the films, namely crystalline structure and tungsten content which are determined by extrinsic parameters such as current density and pH.

The saturation magnetization, M_S, decreases monotonically as the amount of W increases (Fig. 8). A similar trend has been reported for other binary alloys containing a non-ferromagnetic element in solid solution, e.g. Ni–Cu [46] or Fe–Al [47]. This suggests that the dilution mechanism governs the overall magnetization behavior, in agreement with former work on Co–W alloys [11]. The coatings are magnetically isotropic along any in-plane direction since similar hysteresis loops were recorded when applying the field along different in-plane directions. In all cases, the remanence-to-saturation magnetization ratio, M_R/M_S, also termed squareness ratio, measured along the perpendicular-to-plane direction, is lower than for any in-plane direction (Fig. 9). This indicates that a shape anisotropy tends to favor a net in-plane magnetic anisotropy. In addition,

because of the (1 0 0) texture, magnetocrystalline anisotropy does not promote perpendicular-to-plane magnetization either. Indeed, few hcp-Co crystals are oriented with the {0 0 2} planes parallel the substrate plane. Since the {0 0 2} direction is the magnetic easy axis, this means that magnetocrystalline anisotropy favors also in-plane orientation of the magnetization. Remarkably, M_R/M_S progressively decreases with the W content, both along in-plane and perpendicular-to-plane directions.

Similarly, the coercivity, H_C, also decreases with the W content (Fig. 9). Relatively large H_C values are obtained for low W percentages, particularly along the perpendicular-to-plane direction. Indeed, H_C increases from 170 Oe for pure Co films to 470 Oe for films containing 2–3 at.% W. Formation of hard-magnetic hcp Co_3W clusters could be partially responsible for this semi-hard ferromagnetic behavior. Also, enrichment in W at the grain boundaries could induce a decrease of the intergranular dipolar interactions, thus increasing H_C. Interestingly, this moderate coercivity value could be suitable for perpendicular recording media applications, where an exceedingly large coercivity would limit the ability to write the desired magnetic information in the bits. The decrease in H_C and M_R/M_S with the W content could be due to a progressive decrease of the magnetocrystalline anisotropy as the coatings become progressively more nanocrystalline or even amorphous-like.

3.4. Mapping of mechanical properties

Nanoindentation or depth-sensing indentation [48–50] is particularly suitable to assess the mechanical and tribological behavior of electrodeposited coatings. Both the Young's modulus and hardness can be derived from the load versus displacement indentation curves which also contain information on the deformation mechanisms [26]. However, it is still not always straightforward to estimate the intrinsic mechanical properties of a coating from nanoindentation curves because many external and internal factors might influence the collected data [50–52].

In this work, nanoindentation was used to evaluate the influence of solid solution and grain size refining on the mechanical behaviour of Co–W coatings containing a few at.% W up to more than 30 at.% W. In some load–displacement, P–h, curves the loading segments feature the so-called pop-in events (i.e. serrations in the P–h curves), particularly for tungsten contents in the range of 3–19 at.% W (Fig. 10). Such plastic instabilities are not observed on electrodeposited pure Co coatings or

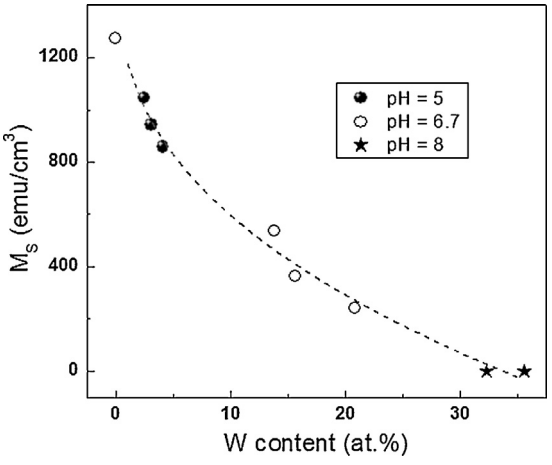

Fig. 8. Dependence of the saturation magnetization, M_S, of Co–W coatings as a function of their W content.

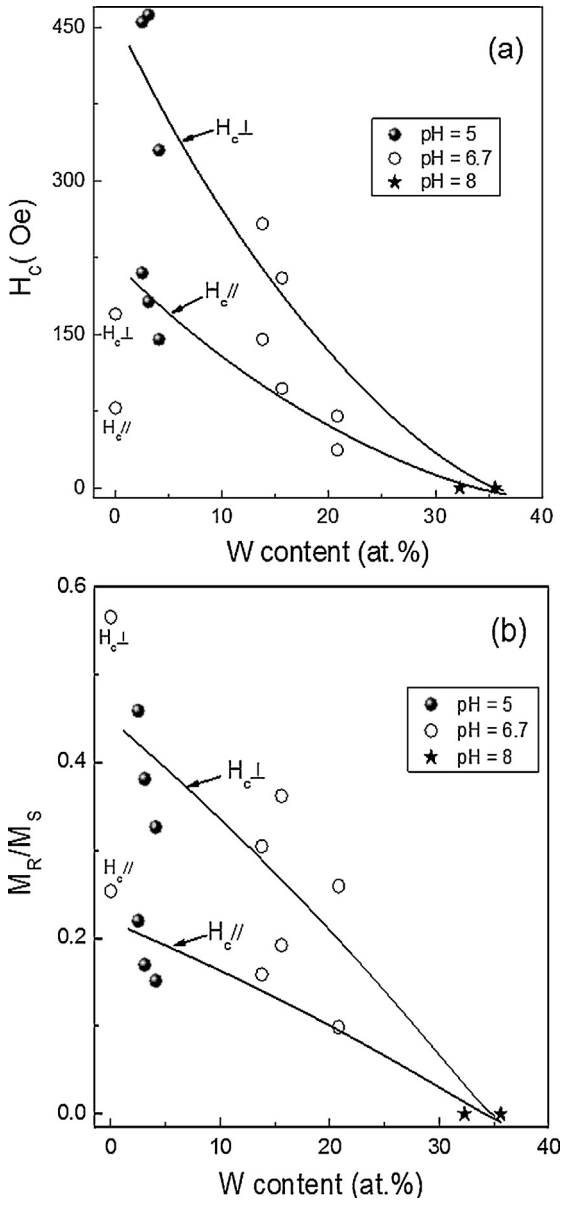

Fig. 9. Dependence of the coercivity, H_C (a), and the squareness ratio, M_R/M_S (b) of Co–W coatings on the at.% W along the in-plane direction and perpendicular-to-plane direction.

Co–W alloys containing a higher tungsten content (i.e. for Co–W deposits exhibiting amorphous-like structure). This is suggesting that their occurrence depends on the electrochemical conditions e.g. current density and, in turn, on the alloy composition and microstructure.

Remarkably, for a given alloy composition and maximum indentation load (e.g. 10 mN), the pop-in appears always close to a critical load, P_c. As can be seen in Fig. 10a, only a slight difference in P_c is observed (P_c = 10.5 mN) for coatings having a similar composition (~3 at.% W obtained at pH 5). Additionally, by comparing the indentation curves obtained at two different maximum loads of 20 mN and 80 mN, an influence of the loading rate on P_c can be inferred (see e.g. Fig. 10a and b for a Co–W coating containing 3 at.% W). The applied loading/unloading rate chosen in the experiments was twice the maximum load per minute. Thus, on applying a higher load (i.e. at 80 mN), nanoindentation was performed at a higher loading/unloading rate (i.e. at 160 mN/min). This dependence of P_c with loading rate indicates the influence of deformation creep

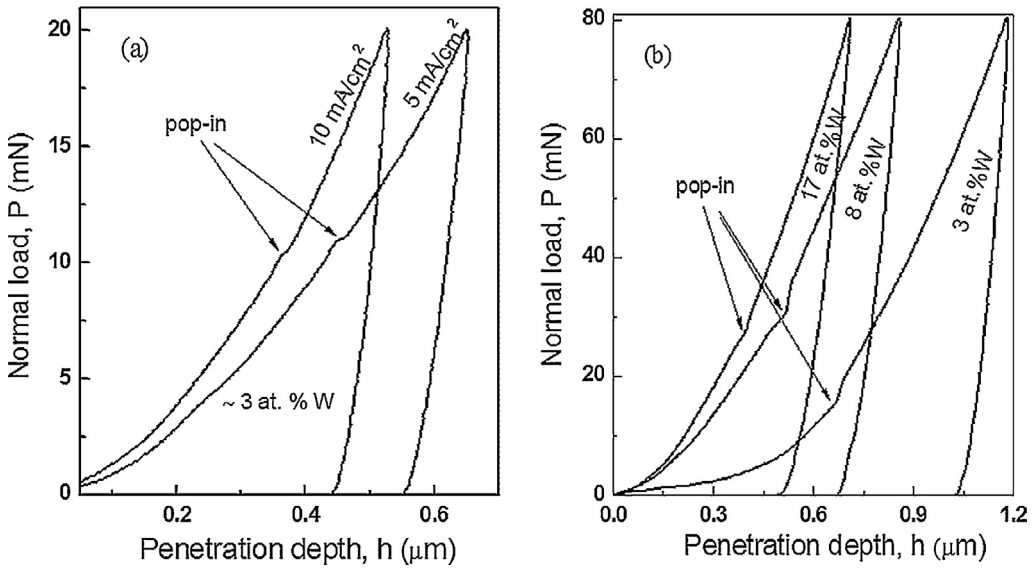

Fig. 10. Nanoindentation curves obtained on Co–W coatings of varying composition.

effects during loading [49]. Our results also indicate that, at a constant strain rate, the critical stress tends to increase with decreasing crystallite size, suggesting that the occurrence of pop-in events is related to a dislocation activity and the interactions with grain boundaries (analogous to the Hall–Petch effect). Serrated plastic flow has been reported for nanocrystalline pure metals and semiconductor single crystals [53], crystalline metallic alloys (e.g. Al–Mg [54]) or even metallic glasses [55].

Interestingly, Fig. 10b also reveals that at 80 mN load, the size of the pop-in event tends to decrease for samples with higher W contents and smaller crystallite sizes. In a first approximation, the length of the instability step, L, can be correlated with the number of generated dislocations as following [56]:

$$L = \frac{d}{2} = \frac{2nA}{\tau} \tag{7}$$

with A a constant, d the grain size, and τ the external stress.

For the most often used Vickers and Berkovich type indenters, the relationship between load, P, and penetration depth, h, for the loading curve the following quadratic function is assumed:

$$P = Ch^2 \tag{8}$$

with C a constant that depends on the geometry of the indenter and the elastic and plastic properties of the material.

However, previous researchers showed that in many cases the loading curve cannot be fitted satisfactorily to a quadratic function, and that a power law approximation has to be used instead [49,50]:

$$P = Ch^m \tag{9}$$

with m usually lower than 2. This observation sometimes is related to the existence of a so-called indentation size effect [49].

As shown in Fig. 11a and b, the loading segments of the indentation curves can be adjusted using Eq. (9). The power exponent m estimated before and after the pop-in events was always found to be lower than 2 and was higher at loads above P_c.

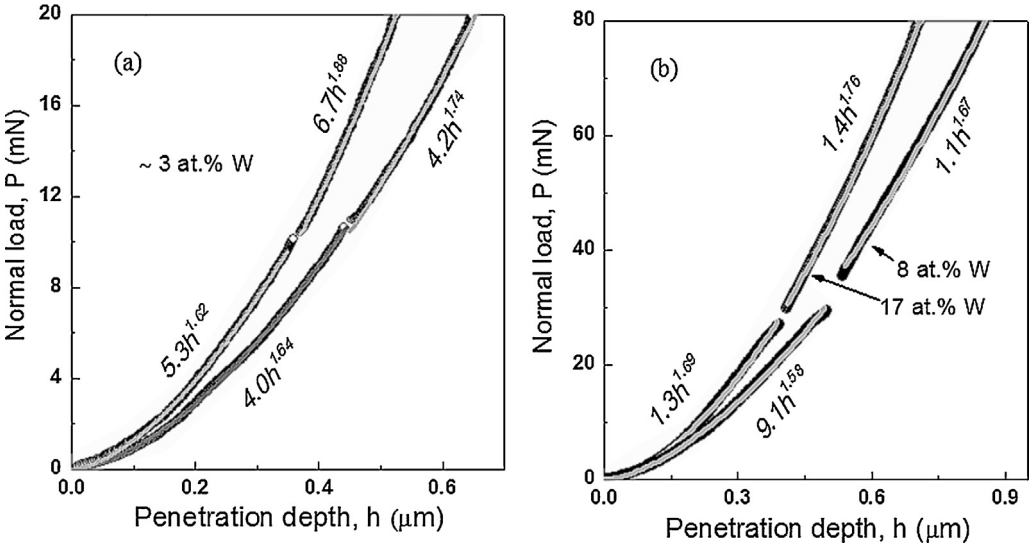

Fig. 11. Loading part of nanoindentation curves recoded on Co–W coatings together with some fits of the loading segments using a power law (see text for details).

This could indicate a plastic hardening induced by dislocation nucleation [53].

There are several theories describing the mechanical response (plastic deformation) of fine-grained and nanocrystalline materials [57]. Such theories consider processes like pile-up breakdown, grain-boundary sliding, core and mantle model, grain boundary dislocation creation and annihilation, grain-boundary rotation, shear band formation, strain gradient model, and mechanical twinning. Some of these models can play an essential role depending on internal/intrinsic (grain size, composition, etc.) or external (temperature, strain rate, stress state) effects. Thus, as shown in [58] the shear stress in nanomaterials depends not only on the material itself but also on its purity, the processing route to obtain nanocrystals, and possible pretreatments.

Tailoring material properties through the control of grain size is crucial for practical applications and it also allows fundamental studies on grain size-dependent physical properties at nanoscale [43,59,60]. Nanohardness of as-deposited Co–W coatings, plotted as a function of their tungsten content, is shown in Fig. 12, together with the corresponding variation of the *E* modulus. The results reveal three issues requiring attention: (i) the hardness of Co–W is lower than that for pure Co when the W content is below 8 at.%; (ii) the hardness increases strongly when the tungsten content increases from 8 to 25 at.% W; (iii) the hardness decreases when the W content exceeds 25 at.%. Most of these observations are related to the intrinsic (microstructural) properties of Co–W coatings. Indeed, it is known that strengthening of nanocrystalline alloys is achieved by the combined effect of solid solution hardening and grain size/boundary strengthening [59]. Here, the presence of a refractory alloying metal, like tungsten causes a substantial increase in the hardness of nanocrystalline Co–W deposits. Simultaneously, a significant decrease in the crystallite size occurred which synergistically increases the hardness in line with Hall–Petch relationship. As a result, the hardness of the Co–W coatings ($H \sim 13$ GPa) is rather high and even comparable to that of pure molybdenum/tungsten films [61], and higher than the one recently reported for Co–W and Ni–Mo alloys [62–65].

The lower hardness of Co–W coatings having low W content, as compared to pure Co, is linked probably to the morphological and textural differences between these coatings, regardless of the similarity in grain size as evaluated from XRD patterns (Fig. 5). Likewise, the decrease in hardness of alloys having a W content above 25 at.%, is probably linked to the transition from the

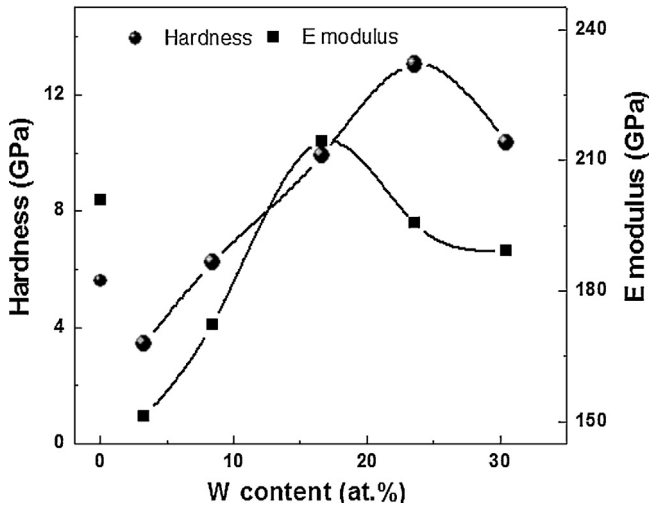

Fig. 12. Mapping of hardness and *E* modulus with the W content of Co–W coatings.

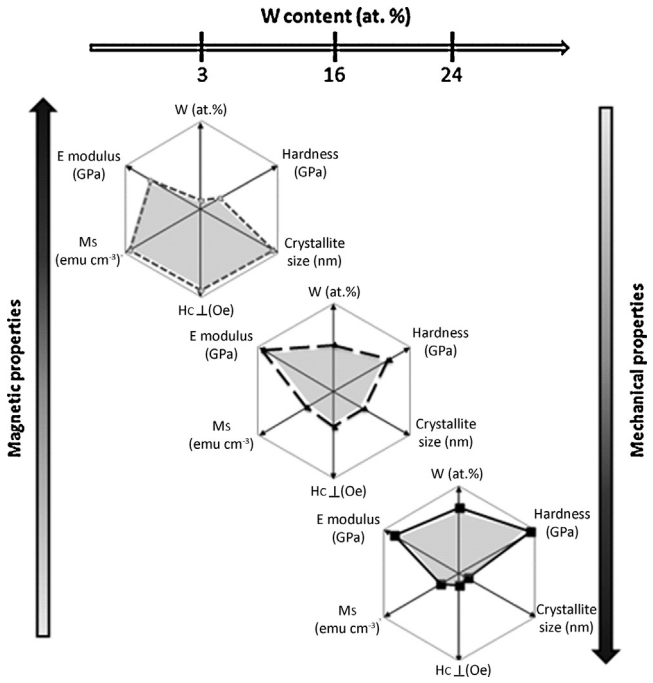

Fig. 13. Mapping chart correlating intrinsic and extrinsic properties of Co–W coatings.

conventional Hall–Petch scaling to breakdown behaviour (inverse Hall–Petch), when the crystallite size falls below 5 nm. A decrease of Young's modulus is also observed at high W contents (Fig. 12). In ultra-nano-crystalline metals and alloys a change in the deformation mechanism from conventional dislocation activity to grain boundary sliding occurs due to the high fraction of intercrystalline material located at grain boundaries [66]. Such regions consist of a disordered structure disposed in a gas-like manner, and possess a lower Young's modulus than the ordered material inside the grains [51]. At a grain size of 5 nm, the intercrystalline volume fraction is approximately 50–80% [51,52]. For intercrystalline fractional volume higher than a critical threshold, grain boundary sliding occurs along suitable intercrystalline planes and hardness decreases with decreasing grain size. The Young's modulus of the investigated Co–W samples as a function of W content shows a maximum at a bit lower W content than where a maximum hardness was noticed. Indeed at a W content of ~17 at.% the Young's modulus starts to decrease. This is probably related to the limited solubility of W in Co (17.5 at.%) [49], and the transition from a crystalline structure in solid solution towards the formation of intermetallic phases or nanosegregation [67]. Furthermore, an increase in porosity associated with the hydrogen evolution during electrodeposition, and the simultaneous rise in W content also could affect the Young's modulus [68,69].

4. Conclusions

The relationships between external growth parameters (bath pH and current density) and intrinsic deposit properties (mainly, tungsten content and crystallite size) have been thoroughly investigated to provide a better understanding of the way how magnetic and mechanical properties of electrodeposited Co–W coatings are correlated. Co–W coatings containing ~2 up to ~36 at.% were deposited galvanostatically from a citrate–borate electrolyte operated at pHs between 5 and 8, and cathodic current densities between 3 and 40 mA cm^{-2}. The increase in W content in Co–W alloys noticed at increasing pH at a given current density, is caused probably by the increase in concentration of the (WO_4)(HCitr)

H^{4-} complex with pH. The incorporation of W into the deposits affects the growth mode, microstructure as well as a concomitant crystallite size.

The mapping of mechanical and magnetic properties of Co–W coatings resulting from this research is summarized in Fig. 13. Based on that mapping, optimization of the tungsten content appears the way to get Co–W electrodeposits with tailored functional properties (hardness, magnetic properties).

Acknowledgements

This work was supported by the FP7 IIF projects NANOALLOY (No. 252407 and 909407) and the FP7 IRSES project TEMADEP (No. 247659). Also, partial funding granted by the MAT2011-27380-C02-01 project funded by Spanish MINECO, the VP1-3.1-ŠMM-08-K-01-014 project funded by Lithuanian ESF agency, the MIP-134 project funded by the Research Council of Lithuania, and the WOG Scientific Network on Surface Modification of Materials funded by FWO-Flanders, is acknowledged.

References

[1] N. Eliaz, E. Gileadi, Induced Co deposition of alloys of tungsten, molybdenum and rhenium with transition metals, in: Modern Aspects of Electrochemistry, vol. 42, Springer, New York, 2008.
[2] E. Lassner, W.D. Schubert, Tungsten – Properties, Chemistry, Technology of the Element, Alloys, and Chemical Compounds, Springer, New York, 1999.
[3] N. Tsyntsaru, H. Cesiulis, M. Donten, J. Sort, E. Pellicer, E.J. Podlaha-Murphy, Modern trends in tungsten alloys electrodeposition with iron group metals, Surface Engineering and Applied Electrochemistry 48 (2012) 491.
[4] N. Sulitanu, F. Brinza, Structure–properties relationships in electrodeposited Ni–W thin films with columnar nanocrystallites, Journal of Optoelectronics and Advanced Materials 5 (2003) 421.
[5] N. Sulitanu, Structural origin of perpendicular magnetic anisotropy in Ni–W thin films, Journal of Magnetism and Magnetic Materials 231 (2001) 85.
[6] N.V. Myung, D.Y. Park, B.Y. Yoo, P.T.A. Sumodjo, Development of electroplated magnetic materials for MEMS, Journal of Magnetism and Magnetic Materials 265 (2003) 189.
[7] N.V. Myung, D.-Y. Park, H. Yang, M. Schwartz, J.W. Judy, C.-K. Yang, K. Nobe, Electrodeposited hard magnetic thin films for MEMS applications, in: Proc. Electrochem. Soc. PV2000-29, 2000, p. 506.
[8] H.H. Yang, N.V. Myung, J. Lee, D.Y. Park, B.Y. Yoo, M. Schwartz, K. Nobe, J.W. Judy, Ferromagnetic micromechanical magnetometer, Sensors and Actuators A 97/98 (2002) 88.
[9] M.E. McHenry, M.A. Willard, D.E. Laughlin, Amorphous and nanocrystalline materials for applications as soft magnets, Progress in Materials Science 44 (1999) 291.
[10] R. Skomski, D.J. Sellmyer, Intrinsic and extrinsic properties of magnetic nanostructures, in: L. Liu, D.J. Sellmyer, D. Shindo (Eds.), Advan Magnetic Mater, Nanostructural Effects, Springer, Berlin, 2006.
[11] U. Admon, M.P. Dariel, E. Grunbaum, J.C. Lodder, Magnetic properties of electrodeposited Co–W thin films, Journal of Applied Physics 62 (1987) 1943.
[12] D.Y. Park, J.M. Ko, Magnetic properties of nanocrystalline Co–W thin film alloys electrodeposited from citrate baths, Journal of Korean Electrochemical Society 6 (2003) 236.
[13] U. Admon, M.P. Dariel, E. Grunbaum, Microstructure of electrodeposited Co–W thin films, Journal of Applied Physics 59 (1986) 2002.
[14] N. Tsyntsaru, A. Dikusar, H. Cesiulis, J.-P. Celis, Z. Bobanova, S. Sidel'nikova, S. Belevskii, Y. Yapontseva, O. Bersirova, V. Kublanovskii, Tribological and corrosive characteristics of electrochemical coatings based on cobalt and iron superalloys, Powder Metallurgy and Metal Ceramics 48 (2009) 419.
[15] A. Bodaghi, J. Hosseini, Corrosion behavior of electrodeposited cobalt–tungsten alloy coatings in NaCl aqueous solution, International Journal of Electrochemical Science 7 (2012) 2584.
[16] N. Tsyntsaru, S. Belevsky, A. Dikusar, J.-P. Celis, Tribological behavior of electrodeposited cobalt–tungsten coatings: dependence on current parameters, Transactions of the Institution of Metal Finishing 86 (2008) 301.
[17] H. Capel, P.H. Shipway, S.J. Harris, Sliding wear behaviour of electrodeposited cobalt–tungsten and cobalt–tungsten–iron alloys, Wear 255 (2003) 917.
[18] F.-J. He, J.-T. Lei, X. Lu, Y.-N. Huang, Friction and wear behavior of electrodeposited amorphous Fe–Co–W alloy deposits, Transactions of Nonferrous Metals Society of China 14 (2004) 901.
[19] F. Su, C. Liu, P. Huang, Establishing relationships between electrodeposition techniques, microstructure and properties of nanocrystalline Co–W alloy coatings, Journal of Alloys and Compounds 557 (2013) 228.
[20] T. Osaka, I. Koiwa, M. Toda, T. Sakuma, T. Namikawa, Y. Yamazaki, Control of thickness dependence of perpendicular coercivity on electroless Co–Ni–Re–P alloy thin films, IEEE Translation Journal on Magnetics in Japan 2 (1985) 208.
[21] T. Shimokawa, T. Yanai, K. Takahashi, M. Nakano, K. Suzuki, H. Fukunaga, Soft magnetic properties of electrodeposited Fe–Ni films prepared in citric acid based bath, IEEE Transactions on Magnetics 48 (2012) 2908.
[22] H. Ge, Q. Wu, G. Wei, X. Wang, Q. Zhou, Effects of bath temperature on electrodeposited permanent magnetic Co-Pt-W(P) films, Bulletin of the Korean Chemical Society 28 (2007) 2214.
[23] J. Aveston, Hydrolysis of tungsten(VI): ultracentrifugation, acidity measurements, and raman spectra of polytungstates, Inorganic Chemistry 3 (1964) 981.
[24] S. Kotrly, L. Šucha, in: R.A. Chalmers, M. Masson (Eds.), Handbook of Chemical Equilibria in Analytical Chemistry, John Wiley, New York, 1985.
[25] J.J. Cruywagen, L. Krüger, E.A. Rohwer, Complexation of tungsten(VI) with citrate, Journal of the Chemical Society, Dalton Transactions 7 (1991) 1727.
[26] W.C. Oliver, G.M. Pharr, Measurement of hardness and elastic modulus by instrumented indentation: advances in understanding and refinements to methodology, Journal of Materials Research 19 (2004) 3.
[27] M. Donten, Bulk and surface composition, amorphous structure, and thermocrystallization of electrodeposited alloys of tungsten with iron, nickel, and cobalt, Journal of Solid State Electrochemistry 3 (1999) 87.
[28] N. Tsyntsaru, J. Bobanova, X. Ye, H. Cesiulis, A. Dikusar, I. Prosycevas, J.-P. Celis, Iron–tungsten alloys electrodeposited under direct current from citrate–ammonia plating baths, Surface and Coatings Technology 203 (2009) 3136.
[29] M.G. Wels, D.A. King, Chemisorption of oxygen on tungsten (1 0 0): combined molecular beam and scanning electron beam study, Journal of Physics C: Solid State Physics 7 (1974) 4053.
[30] H. Cesiulis, X.G. Xie, E.J. Podlaha-Murphy, Electrodeposition of Co–W alloys with P and Ni, Materials Science (Medziagotyra) 15 (2009) 115.
[31] N. Tsyntsaru, H. Cesiulis, A. Budreika, X. Ye, R. Juskenas, J.-P. Celis, The effect of electrodeposition conditions and post-annealing on nanostructure of Co–W coatings, Surface and Coatings Technology 206 (2012) 4262.
[32] M. Donten, Z. Stojek, H. Cesiulis, Formation of nanofibers in thin layers of amorphous W alloys with Ni, Co, and Fe obtained by electrodeposition, Journal of the Electrochemical Society 150 (2003) C95.
[33] M. Donten, H. Cesiulis, Z. Stojek, Electrodeposition of amorphous/nanocrystalline and polycrystalline Ni–Mo alloys from pyrophosphate baths, Electrochimica Acta 50 (2005) 1405.
[34] M. Donten, Z. Stojek, Pulse electroplating of rich-in-tungsten thin layers of amorphous Co–W alloys, Journal of Applied Electrochemistry 26 (1996) 665.
[35] H. Wang, R. Liu, F. Cheng, Y. Cao, G. Ding, X. Zhao, Electrodepositing amorphous Ni–W alloys for MEMS, Microelectronic Engineering 87 (2010) 1901.
[36] D.P. Weston, S.J. Harris, P.H. Shipway, N.J. Weston, G.N. Yap, Establishing relationships between bath chemistry, electrodeposition and microstructure of Co–W alloy coatings produced from a gluconate bath, Electrochimica Acta 55 (2010) 5695.
[37] R. Juskenas, I. Valsiunas, V. Pakstas, R. Giraitis, On the state of W in electrodeposited Ni–W alloys, Electrochimica Acta 54 (2009) 2616.
[38] A. Guinier, X-ray Diffraction in Crystals, Imperfect Crystals, and Amorphous Bodies, Dower Publications, New York, 1994.
[39] G. Herzer, Grain Size dependence of coercivity and permeability in nanocrystalline ferromagnets, IEEE Transactions on Magnetics 26 (1990) 1397.
[40] D.H. Jeong, F. Gonzalez, G. Palumbo, K.T. Aust, U. Erb, The effect of grain size on the wear properties of electrodeposited nanocrystalline nickel coatings, Scripta Materialia 44 (2001) 493.
[41] D.H. Jeong, U. Erb, K.T. Aust, G. Palumbo, The relationship between hardness and abrasive wear resistance of electrodeposited nanocrystalline Ni–P coatings, Scripta Materialia 48 (2003) 1067.
[42] Z. Zhang, F. Zhou, E.J. Laverina, On the analysis of grain size in bulk nanocrystalline materials via X-ray diffraction, Metallurgical and Materials Transactions A 34A (2003) 1349.
[43] A.J. Detor, C.A. Schuh, Tailoring and patterning the grain size of nanocrystalline alloys, Acta Materialia 55 (2007) 371.
[44] I. Mizushima, Electrodeposition of Ni–W alloy and characterization of Microstructure and properties of the deposits, PhD Thesis, 2006.
[45] B.E. Warren, J. Biscce, The structure of silica glass by X-ray diffraction studies, Journal of the American Ceramic Society 21 (1938) 49.
[46] E. Pellicer, A. Varea, S. Pané, B.J. Nelson, E. Menéndez, M. Estrader, S. Suriñach, M.D. Baró, J. Nogués, J. Sort, Nanocrystalline electroplated Cu–Ni: metallic thin films with enhanced mechanical properties and tunable magnetic behavior, Advanced Functional Materials 20 (2010) 983.
[47] J. Nogués1, E. Apiñaniz, J. Sort, M. Amboage, M. d'Astuto, O. Mathon, R. Puzniak, I. Fita, J.S. Garitaonandia, S. Suriñach, J.S. Muñoz, M.D. Baró, F. Plazaola, F. Baudelet, Volume expansion contribution to the magnetism of atomically disordered intermetallic alloys, Physical Review B 74 (2006) 024407.
[48] J.R. Greer, J.T.M. de Hosson, Plasticity in small-sized metallic systems: intrinsic versus extrinsic size effect, Progress in Materials Science 56 (2011) 654.
[49] N.Q. Chinh, J. Gubicza, Z. Kovács, J. Lendvai, Depth-sensing indentation tests in studying plastic instabilities, Journal of Materials Research 19 (2004) 31.
[50] C. Lu, Y.-W. Mai, P.L. Tam, Y.G. Shen, Nanoindentation-induced elastic–plastic transition and size effect in α-Al_2O_3 (0 0 0 1), Philosophical Magazine Letters 87 (2007) 409.
[51] Y.T. Cheng, C.M. Cheng, Scaling, dimensional analysis, and indentation measurements, Materials Science and Engineering Reports 44 (2004) 91.
[52] C.A. Schuh, Nanoindentation studies of materials, Materials Today 9 (2006) 32.
[53] D. Lorenz, A. Zeckzer, U. Hilpert, Pop-in effect as homogeneous nucleation of dislocations during nanoindentation, Physical Review B 67 (2003) 172101.

[54] G. Bérces, N.Q. Chinh, A. Juhász, J. Lendvai, Kinematic analysis of plastic instabilities occurring in microhardness tests, Acta Materialia 46 (1998) 2029.
[55] A. Concustell, J. Sort, G. Alcalá, S. Mato, A. Gebert, J. Eckert, M.D. Baró, Plastic deformation and mechanical softening of $Pd_{40}Cu_{30}Ni_{10}P_{20}$ bulk metallic glass during nanoindentation, Journal of Materials Research 20 (2005) 2719.
[56] B. Yang, H. Vehoff, Grain size effects on the mechanical properties of nanonickel examined by nanoindentation, Materials Science and Engineering A 400/401 (2005) 467.
[57] M.A. Meyers, A. Mishra, D.J. Benson, Mechanical properties of nanocrystalline materials, Progress in Materials Science 51 (2006) 427.
[58] S. Takeuchi, The mechanism of the inverse Hall–Petch relation of nanocrystals, Scripta Materialia 44 (2001) 1483.
[59] C.A. Schuh, T.G. Nieh, H. Iwasaki, The effect of solid solution W additions on the mechanical properties of nanocrystalline Ni, Acta Materialia 51 (2003) 431.
[60] L.P. Bicelli, B. Bozzini, C. Mele, L. D'Urzo, A review of nanostructural aspects of metal electrodeposition, International Journal of Electrochemical Science 3 (2008) 356.
[61] S. Eroglu, H. Ekren, T. Baykara, Surface hardening of tungsten heavy alloys, Scripta Materialia 38 (1997) 131.
[62] F.-H. Su, P. Huang, Microstructure and tribological property of nanocrystalline Co–W alloy coating produced by dual-pulse electrodeposition, Materials Chemistry and Physics 134 (2012) 350.
[63] E. Beltowska-Lehman, A. Bigos, P. Indyka, M. Kot, Electrodeposition and characterisation of nanocrystalline Ni–Mo coatings, Surface and Coatings Technology 211 (2012) 67.
[64] F.-H. Su, C.-S. Liu, P. Huang, Effect of complexing agents and pH on microstructure and tribological properties of Co–W coatings produced by double pulse electrodeposition, Applied Surface Science 258 (2012) 6550.
[65] M. Mulukutla, V.K. Kommineni, S.P. Harimkar, Pulsed electrodeposition of Co–W amorphous and crystalline coatings, Applied Surface Science 258 (2012) 2886.
[66] J.R. Trelewicz, C.A. Schuh, The Hall–Petch breakdown in nanocrystalline metals: a crossover to glass-like deformation, Acta Materialia 55 (2007) 5948.
[67] J.R. Trelewicz, C.A. Schuh, Grain boundary segregation and thermodynamically stable binary nanocrystalline alloys, Physical Review B 79 (2009) 094112.
[68] M. Aliofkhazraei, Nanocoatings, Engineering Materials, Springer-Verlag, Berlin Heidelberg, 2011.
[69] E. Pellicer, S. Pané, V. Panagiotopoulou, S. Fusco, K.M. Sivaraman, S. Suriñach, M.D. Baró, B.J. Nelson, J. Sort, Localized electrochemical deposition of porous Cu–Ni microcolumns: insights into the growth mechanisms and the mechanical performance, International Journal of Electrochemical Science 7 (2012) 4014.